Journal of Energy Storage 101 (2024) 113866

Contents lists available at ScienceDirect

Journal of Energy Storage

journal homepage: www.elsevier.com/locate/est

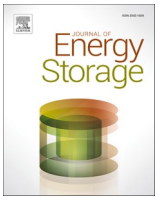

Research papers

High-uniformity liquid-cooling network designing approach for energy storage systems by graph-coupled genetic algorithm

Huaiyu Zuo, Jiacheng Han, Song Xue, Zhaochen Wang, Zeyu Wang, Run Hu, Jinlong Ma, Xiaobing Luo *

School of Energy and Power Engineering, Huazhong University of Science and Technology, Wuhan 430074, China

ARTICLE INFO

Keywords:
Design optimization
Liquid-cooling network
Battery energy storage system
Battery thermal management

ABSTRACT

Electrochemical battery energy storage stations have been widely used in power grid systems and other fields. Controlling the temperature of numerous batteries in the energy storage station to be uniform and appropriate is crucial for their safe and efficient operation. Thus, effective thermal management is required. In this work, an approach for rapid and efficient design of the liquid cooling system for the stations was proposed. A hydraulic solution model for the liquid-cooling network was established based on graph theory principles, and the genetic algorithm was employed for automatic system optimization to achieve high cost-effectiveness and ideal temperature distribution. Experiments were conducted to validate the accuracy of the hydraulic model and evaluate the efficacy of the optimization strategy. The flow rate calculated from the hydraulic model agreed well with the experiments, with a discrepancy smaller than 3.5 %, and the uniformity of flow rates was improved to as high as 70 % after the optimization. Furthermore, the applicability of this approach was also confirmed across various sizes of energy storage systems.

1. Introduction

As electrochemical energy storage technology has advanced, container battery energy storage stations (BESS) have gained popularity in power grids [1,2]. Their advantages, such as reduced land use, easy installation, and mobility, make them effective and flexible in balancing energy demand and supply over time [3,4]. Since the performance of batteries in BESSs depends heavily on the reaction temperature due to internal electrochemical processes [5,6], the battery thermal management system (BTMS) is crucial in container BESSs [7]. It plays a vital role in ensuring both safety and efficiency [8,9]. One function of BTMS is to maintain the temperature of every battery within an appropriate range (20 °C–40 °C), which promotes system efficiency and prevents potential safety hazards associated with thermal runaway of batteries [10,11]. Large temperature differences between battery packs will lead to battery capacity loss [12], further reducing the lifespan of the energy storage stations. Thus, the other important function of BTMS is to maintain temperature consistency across different battery packs, with the temperature differences typically below 5 °C [13]. Considering the energy consumption of BTMS itself, designing BTMS presents a significant challenge as it must ensure that the BESS operates at a uniform and suitable temperature while maintaining low manufacturing and operating costs.

Among various BTMS solutions, liquid cooling plate system stands out for BESS thermal management as the size of container BESS and battery capacities continue to increase [14]. This strategy offers precise and efficient heat dissipation capabilities [15], optimal security and preferable cost-effectiveness. Compared to air cooling, which can cause local hot spots [16], and immersion liquid cooling, which presents higher safety risks [17], as well as other strategies [18], liquid cooling plate cooling is a superior alternative. This makes it conducive to ensuring the long-term feasibility of BESSs. Liquid cooling plate system comprises of liquid cooling plates (LCP) and suited liquid-cooling network. In its design, two primary challenges must be addressed to achieve the thermal management target mentioned above. The first one involves controlling the temperature distribution in the individual battery pack, which requires meticulous design of LCPs. To date, a series of studies focused on the design and optimization of LCP have been reported. Deng et al. proposed a cold plate with serpentine-channel configuration, and studied the impact of channel number, channel layout and coolant inlet temperature on the cooling performance [19]. Researchers have also investigated cold plates with various geometrical

* Corresponding author.
E-mail address: luoxb@hust.edu.cn (X. Luo).

https://doi.org/10.1016/j.est.2024.113866
Received 10 May 2024; Received in revised form 6 September 2024; Accepted 19 September 2024
Available online 27 September 2024

configurations and structures. For instance, Zhang et al. introduced a biomimetic design inspired by the fin structure of horseshoe crabs for liquid cooling systems. This design, optimized through multi-objective techniques, demonstrated significant performance enhancements [20]. Additionally, other studies have explored butterfly-shaped, pin-shaped col. plates and bi-functional heating-cooling plates, analyzing their heat dissipation capabilities [21–24]. Meanwhile, researchers proposed an advancing model for liquid cold plates. Zhang et al. introduced a comprehensive computational method for total thermal resistance and pressure loss of liquid-cooled battery thermal management system [25].

The second one involves achieving temperature uniformity across different battery packs in the whole system. BESSs typically feature parallel liquid cooling networks, in which the inlet liquid temperatures for each LCP are the same and the temperature distribution in each battery pack is closely linked to the flow rate through each LCP. Therefore, ensuring uniform flow into each LCP is imperative for maintaining system-wide temperature uniformity. However, the challenge of keeping flow uniformity between LCPs is complex. Due to the spatial distribution of battery packs and the flow resistance loss of pipe network, the flow distribution between cold plates is extremely uneven [26,27], which further impacts the battery life and system performance [28,29]. Current research and technology focusing on this issue predominantly rely on direct design pipe network using computational fluid dynamics (CFD) simulation [30] and manual adjustment of CFD models [31,32]. Additionally, there is ongoing research into maintaining dynamic monitoring during system operation [33]. Zhang et al. proposed a manual CFD method for analyzing and resolving this issue, but this approach is inefficient and unsuitable for coping with complex system [34]. Pistoresi et al. used optimized tapered pipes to improve flow distribution uniformity [35]. However, the high cost of irregularly shaped pipelines in practical applications, combined with their limitations under off-design conditions, makes this approach less feasible. Chen et al. proposed an optimization method for uniform flow distribution in the manifold of server cabinets, but has limitations in single-stage, fixed-structure [36]. Therefore, it is imperative to develop and implement rapid design and optimization methods for thermal distribution in BESSs.

In this work, a liquid-cooling network designing approach (LNDA) was proposed for thermal management in BESSs. Our approach was devised to efficiently construct liquid-cooling networks specifically tailored for diverse scale BESSs, with considerations of cost-effectiveness, energy efficiency, performance, and consistency. First, a mathematical model was established for the liquid-cooling network of BESS. This model integrated graph theory principles to arrange and solve the equilibrium equation governing the pipeline network, thereby obtaining comprehensive hydraulic performance of the network. The LNDA coupled the proposed model with a genetic algorithm (GA) to optimize various parameters. This included determining the diameter and length of each pipeline, as well as number, and placement of booster pumps, and determining the most favorable valve openings. Consequently, this facilitated the operation of individual battery packs at their ideal temperatures while ensuring uniform cooling across the entirety of the battery system and minimizing associated costs. Additionally, the accuracy of the model and efficacy of LNDA were validated and assessed by extensive experiments and numerous case studies. Our approach furnished an efficient and pragmatic solution for the design of liquid-cooling system within BESSs.

2. Method

The schematic diagrams depicted in Fig. 1a illustrate the configuration of the container lithium-ion battery energy storage station along with its liquid-cooling system. Multiple battery packs are integrated into the BESS, each requiring efficient heat dissipation. Consequently, a

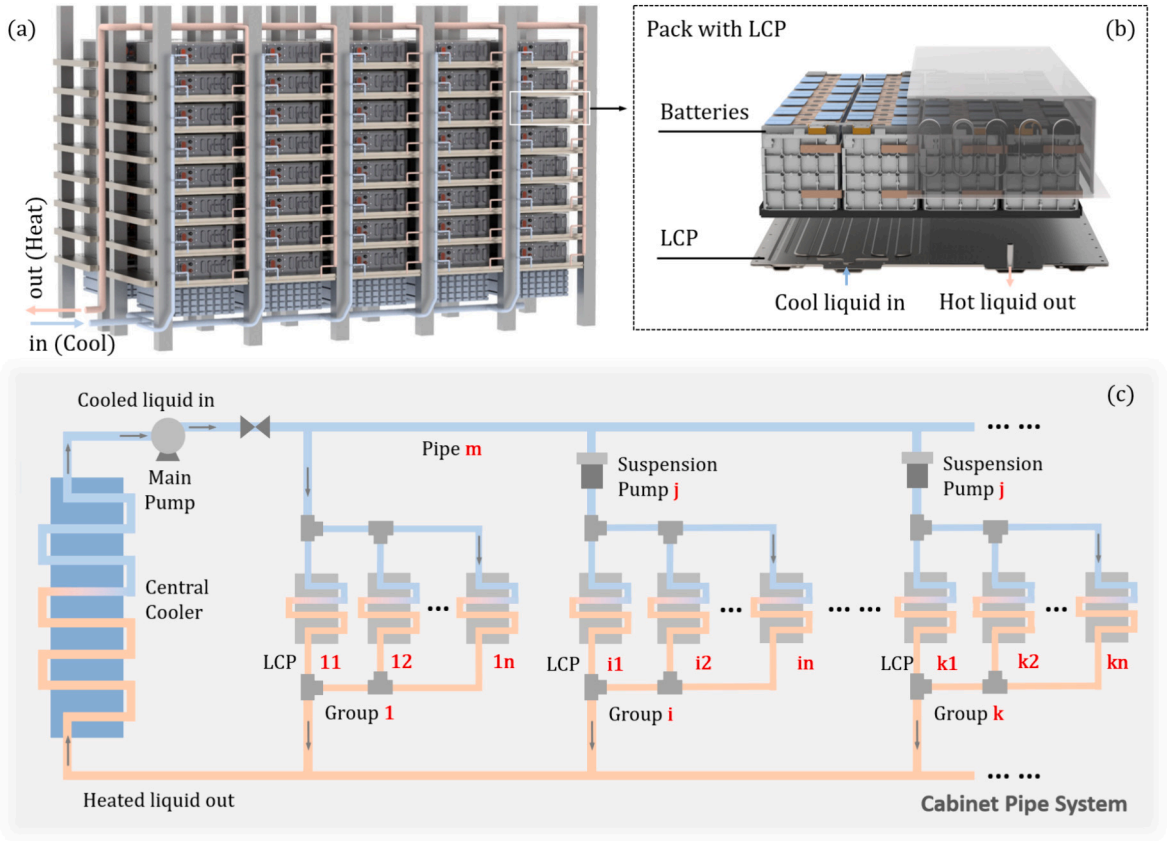

Fig. 1. (a) Lithium-ion BESS with BMTS (formed by LCPs and pipeline networks) (b) single pack with its LCP (c) Simplified diagram of the whole system.

dedicated LCP (as shown in Fig. 1b) is allocated to each battery pack. These cold plates are interconnected by an intricate network of pipes, forming a comprehensive pipeline network. The pipeline network and LCPs constitute the thermal management system, whose operational principles are presented in Fig. 1c. Here, the working medium undergoes heat exchange within the cooler, subsequently being pressurized by the primary pump of the pipeline network. It then circulates along the pipeline and enters LCPs, where it engages in heat exchange with the batteries, thereby effectuating cooling. The heated working medium is then redirected back to the cooler, where it completes the cycle of the liquid cooling system.

2.1. Hydraulic solution model of the pipeline network

A high-precision hydraulic solution model for the network is constructed to address the hydraulic characteristics of each segment of the pipe network. The model works as the base of the LNDA. The solution steps are as follows: 1. Establish the mathematical structure of the pipe network 2. Formulate the governing physical Eq. (3). Simplify the equations using graph theory. 4. Iteratively solve the equations to determine the hydraulic characteristics of the network. When the battery pack index and arrangement mode are obtained, the mathematical graph of parallel liquid-cooling network is constructed according to the information (Fig. S1.1).

2.1.1. Governing equations

With this graph, the model is built based on the pipeline network balance laws, comprising the node flow balance law and the loop pressure balance law. The node flow balance law (Eq. (1)) ensures that the net flow into or out of a node in the pipeline network is zero [37,38], as

$$\sum_{j=1}^{n} b_{kj} Q_j = 0 \ (k = 1, 2, \ldots, m-1) \tag{1}$$

where, n represents the number of pipelines in the network, and m is the number of nodes. b_{kj} is the directional characteristic coefficient of the flow rate to the node k in the pipeline j. When the liquid flows into the node in the pipeline, $b_{kj} = 1$, when it flows out, $b_{kj} = -1$, and when the pipeline is not connected with the node $b_{kj} = 0$. Q_j is the flow rate of this pipeline j.

The loop pressure balance law (Eq. (2)) guarantees that the net pressure around a loop in the pipeline network is zero, as

$$\sum_{j=1}^{n} C_{ij}\left(S_j {Q_j}^2 - H_{fj} - H_{Nj}\right) = 0 \ (i = 1, 2, \ldots, n-m+1) \tag{2}$$

where, n-m + 1 represents the number of independent loops in the network. C_{ij} is the directional characteristic coefficient of the flow rate to the loop i in the pipeline j. When the flow in the pipeline has the same direction with the loop, $C_{ij} = 1$, when they are opposite, $C_{ij} = -1$, and when the pipeline is out of the loop $C_{ij} = 0$. S_j is the drag coefficient of this pipeline j. H_{fj} is the pump lift in the pipeline where the main/booster pumps are located.

2.1.2. Simplification and selection of equations

The liquid-cooling networks of BESSs are extensively complex (Fig. 1c). It contains many nodes and branches, which results in a large number of equations according to Eqs. (1) and (2). Therefore, directly solving these equations is hindered by over-constraint and over-load of computations. To overcome these issues, the principles of graph theory are adopted to select, simplify and arrange the system equations. The graph-based process identifies independent loops within the pipeline network to establish equations. Then, by solving these equations, the flow and head variables for each necessary pipeline and node can be calculated respectively.

To illustrate the loop selection process, a typical pipeline network structure (Fig. 1a: 5 rows, 8-layer battery packs each row) is handled and depicted in Fig. 2. Initially, a basic graph is created, consisting of nodes and branches within the pipeline network (Fig. 2.1). The Kruskal algorithm is then applied to identify the spanning tree of the graph (Fig. 2.2), which establishes a path connecting all nodes without forming a loop [39]. This spanning tree significantly simplifies the problem. According to the graph theory, whenever an additional edge is added, loops are formed, and these loops are independent with each other [40]. The backtracking method [41] is employed to discover all independent loops in the network (Fig. 2.3). Based on these independent loops, the nonlinear equations of loop pressure balance for the overall pipeline system can be established as follows [42,43].

$$f_i\left(q_{y1}, q_{y2}, \ldots, q_{y(n-m+1)}\right) = \sum_{j=1}^{n} C_{ij}\left(s_j {q_j}^2 - h_{fj} - h_{Nj}\right) = 0 \ (i = 1, 2, \ldots, n-m+1) \tag{3}$$

where, $q_{y1}, q_{y2}, \ldots, q_{y(n-m+1)}$ represents the flow rates in edges of a cotree.

2.1.3. Iterative solution

Assuming the non-linear equations have been iterated k times, the approximation of the flow rates at k-th time can be obtained (Eq. (4)):

$$Q_Y^{k^T} = \left[{q_{y1}}^k, {q_{y2}}^k, \ldots, {q_{y(n-m+1)}}^k\right] \tag{4}$$

Perform a Taylor expansion of Eq. (3) and neglect its higher-order terms beyond the second order. Neglecting higher-order terms is justified as the retained terms provide the most significant contribution to the function's value, facilitating equation simplification and computational efficiency. The (k + 1)-th linearization approximation of equations can be written as follows.

$$f_i\left({q_{y1}}^{k+1}, {q_{y2}}^{k+1}, \ldots, {q_{y(n-m+1)}}^{k+1}\right) = f_i\left({q_{y1}}^k, {q_{y2}}^k, \ldots, {q_{y(n-m+1)}}^k\right) + \frac{\partial f_i}{\partial q_{y1}} \Delta {q_{y1}}^k + \frac{\partial f_i}{\partial q_{y2}} \Delta {q_{y1}}^k + \ldots + \frac{\partial f_i}{\partial q_{y(n-m+1)}} \Delta {q_{y1}}^k \tag{5}$$

where, $\Delta {q_{yi}}^k$ represents the k-th correction value of the flow rate, where

$$\Delta {q_{yi}}^k = {q_{yi}}^{k+1} - {q_{yi}}^k \tag{6}$$

Thus, the Eq. (5) can be transformed into the matrix form (Eq. (7)).

$$\begin{bmatrix} \frac{\partial f_1}{\partial q_{y1}} & \frac{\partial f_1}{\partial q_{y2}} & \cdots & \frac{\partial f_1}{\partial q_{y(n-m+1)}} \\ \frac{\partial f_2}{\partial q_{y1}} & \frac{\partial f_2}{\partial q_{y2}} & \cdots & \frac{\partial f_2}{\partial q_{y(n-m+1)}} \\ \vdots & & \ddots & \vdots \\ \frac{\partial f_{(n-m+1)}}{\partial q_{y1}} & \frac{\partial f_{(n-m+1)}}{\partial q_{y2}} & \cdots & \frac{\partial f_{(n-m+1)}}{\partial q_{y(n-m+1)}} \end{bmatrix} \begin{bmatrix} \Delta {q_{y1}}^k \\ \Delta {q_{y2}}^k \\ \Delta {q_{y3}}^k \\ \Delta {q_{y4}}^k \\ \vdots \\ \Delta {q_{y(n-m+1)}}^k \end{bmatrix} = - \begin{bmatrix} {f_1}^k \\ {f_2}^k \\ {f_3}^k \\ {f_4}^k \\ \vdots \\ {f_{(n-m+1)}}^k \end{bmatrix} \tag{7}$$

With the hypothesis that the main diagonal is dominant, the Eq. (7) can be simplified to the following form.

$$\Delta {q_{yi}}^k = -\frac{f_i^k}{\frac{\partial f_i}{\partial q_{yi}}} \tag{8}$$

By substituting the cotree flow balance equation and finding the partial derivative of q_{yi} for f_i, the first-order infinitesimal $\Delta {q_{yi}}^k$ is eventually described as follows (Eq. (11)):

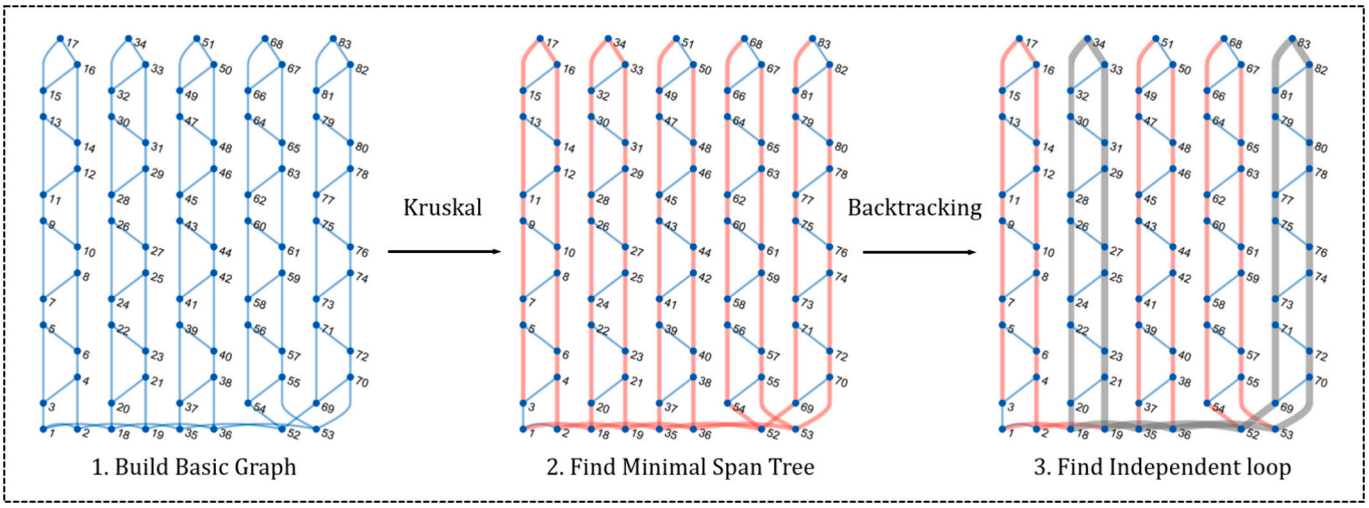

Fig. 2. The process of finding all independent loops of the pipeline network.

$$q_j = \sum_{l=1}^{n-m+1} C_{lj} q_{yl} \tag{9}$$

$$\frac{\partial f_i}{\partial q_{yi}} = \sum_{j=1}^{n} C_{ij}{}^2 \left(2 s_j q_j - \frac{dh_{fj}}{dq_j} \right) \tag{10}$$

$$\Delta q_{yi}{}^k = - \frac{\sum_{j=1}^{n} C_{ij} \left(s_j q_j{}^2 - h_{fj} - h_{Nj} \right)}{\sum_{j=1}^{n} C_{ij}{}^2 \left(2 s_j q_j - \frac{dh_{fj}}{dq_j} \right)} \tag{11}$$

For each independent loop, a flow correction value Δq_{yi} is obtained during each iteration. Therefore, it is necessary to set a desired value of solution accuracy ε. When the flow correction value for each loop falls below the specified solution accuracy, the solution process converges (Eq. (12)). At convergence, the data for the head of each node and the flow rate of each pipeline in the pipeline network can be obtained.

$$max \left| \Delta q_{yi} \right| < \varepsilon \tag{12}$$

Through the meticulous identification of independent loops in the pipeline network and subsequent solution of the associated equations, the hydraulic solution model for the pipeline network is constructed. Leveraging this model, the calculation of key parameters (including the head of each node and the flow rate of each pipe) in the network is conducted with high efficiency and accuracy.

2.2. Liquid-cooling network designing approach

Based on the hydraulic solution model of the liquid-cooling network, the optimization algorithm is employed to facilitate the LNDA. The key of LNDA consists of the optimized parameters, constrained conditions, objective function and the optimization process.

2.2.1. Optimized parameters

The key factors which impact the hydraulic performance of the pipeline network are identified according to the explanation of the drag coefficient s_j [44],

$$s_j = \frac{2\lambda \cdot l_j}{\pi g \cdot D_j{}^3} + \frac{\zeta}{2g \cdot x_j{}^2} \quad j = 1, 2, 3 \ldots, n \tag{13}$$

where, l_j represents the length of the pipeline j while D_j is the diameter. λ, ζ are determined by Colebrook-White diagram and engineering estimate, containing factors such as fluid type, pipe shape, material, roughness, and temperature. The optimization includes the geometry parameters D and l of pipelines. Moreover, valves are applied in the network to adjust the flow distribution as its affect described in the second item of Eq. (13). x_j is the opening value of valves, the range of which is from 0 to 1, with 0 representing valve full-off, and 1 representing full-open (Fig. 3a). Additionally, the booster pumps are adopted in the network to improve hydraulic performance. The optimized parameters contain their quantity and locations (Fig. 3b). The location item serves as a pointer, enabling the code to automatically incorporate the hydraulic matrix of the booster pump into the respective pipeline. The hydraulic performance of booster pump can be written as $\Delta H_{P_i} = A_b \cdot Q_{P_i}{}^2 + B_b \cdot Q_{P_i} + C_b$. The form of the optimized parameter in the code is $\left[D_{1,2,3}, L_{1,2,\ldots,n}, V_{1,2,\ldots N_v}, N_p, P_{1,2\ldots N_p} \right]$. Additionally, to address potential pump force inadequacy, we adjust it by automatically increasing the constant term of the head curve of the main pump in the calculation. Particularly, in the pipeline where LCPs are located, the drag coefficient should be replaced by the drag coefficient matrix of the LCP. Table 1 presents a comprehensive dataset concerning basic pipeline network, experiments and optimization.

2.2.2. Parameter constraints and evaluation

Prior to optimization, it is imperative to impose constraints on the geometric dimensions of pipeline length and diameter. Due to the engineering nature of pipeline network design, nominal industrial pipe-diameters are adopted for ease of implementation. Hence, the pipe diameter selection is limited to the series of values provided by the industrial pipes. Additionally, the pipe-length influences system performance and spatial size of integrated energy storage stations. Therefore, the length ranges of different hierarchical pipelines across various rows and layers are carefully valued as CONSTRAINT 1. It contains the information of $LR_{imin} \le l_i \le LR_{imax}$ and $D_i \in [DR_{i1}, \ldots, DR_{ik}]$.

Simultaneously, an evaluation process must be conducted to ensure the optimized parameters can satisfy the conditions for the calculated hydraulic results within the pipe network, as well as the temperature difference requirements between the battery packs. This evaluation process is expressed as CONSTRAINT 2 in the code. The hydraulic constraint necessitates that the liquid head h_i at each node in the pipe network exceeds 0, under which circumstance the flow can reach out to this point. Meanwhile, the flow rate through each LCP Q_{LCP_i} must surpass the minimal required flow rate Q_{iReq} for effective and uniform heat dissipation. Additionally, the maximum deviation of flow rates through all LCPs $\left[\left(Q_{LCP_i} \right)_{max} - \left(Q_{LCP_i} \right)_{min} \right]$ should be less than maximal tolerated

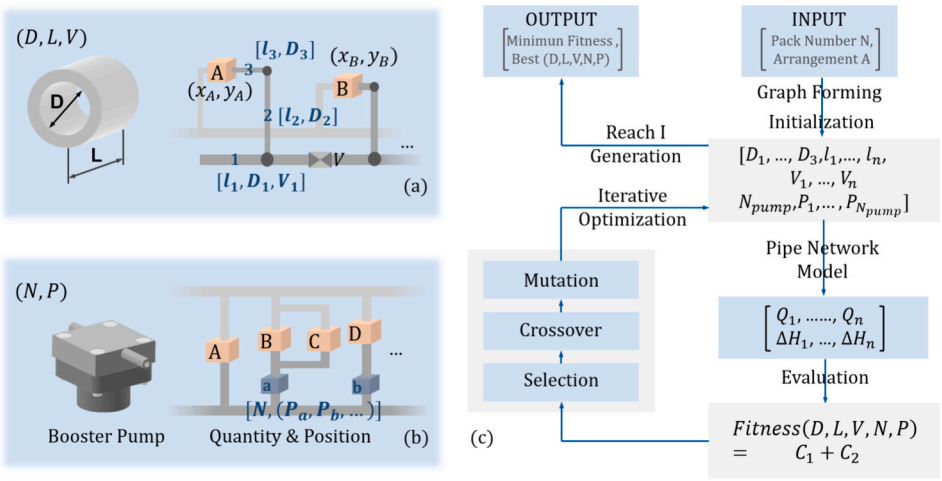

Fig. 3. (a-b) Description of optimized parameters. (c) Flow chart of design and optimization of the LNDA.

Table 1
Comprehensive characteristics and dataset.

Parameter	Symbol	Value
Pipeline network geometry parameters		
Number of batteries	N	–
Number of battery array set	s	–
Number of nodes	m	$2s+2N$
Number of pipelines	n	$2s-1+3N$
Number of independent loops	$n-m+1$	N
Experiment		
Length (of pipeline with main pump)	L_j	1200±20 mm
Length (of primary pipeline)	L_j	200±10 mm
Length (of secondary pipeline)	L_j	150±5 mm
Inner diameter (of primary pipeline)	D_j	25 mm
Inner diameter (of secondary pipeline)	D_j	10 mm
Drag coefficient (of primary pipeline)	λ_{p1}	3.93×10^{-4} m/(L/min)^2
Drag coefficient (of secondary pipeline)	λ_{p2}	5.13×10^{-4} m/(L/min)^2
Length of LCP	L_{LCP}	400 mm
Width of LCP	W_{LCP}	300 mm
Size of the cabinet	–	$1800\times600\times600$ mm^3
Height of the single step	–	200 mm
Optimization operating conditions		
Population quantity	N	100
Iterations	It	50/60/70
Catastrophe probability	mut	0.4
Cross probability	acr	0.5
Length range (of primary pipeline)	L_j	1–2 m
Length range (of secondary pipeline)	L_j	0.3–0.5 m
Diameter range (of primary pipeline)	D_j	50–90 mm
Diameter range (of secondary pipeline)	D_j	20–30 mm
Diameter range (of tertiary pipeline)	D_j	8–15 mm
Solution accuracy	ε	0.001
Objective function		
Annual interest rate of network	r	0.6
Investment recovery time	t	5
Pump efficiency (main/booster)	η_p	70 %/60 %
annual working hours	τ	8640 h
Average electricity fee (Wuhan, China)	c_e	0.86 CNY/kWh

difference ΔQ_{Tol}. This constraint serves a dual purpose by ensuring the seamless coordination of the system's charging and discharging processes, while improving its overall service life. Therefore, CONSTRAINT 2 includes the information of $h_i > 0, Q_{LCP_i} > Q_{iReq}$ and $\left[\left(Q_{LCP_i}\right)_{max} - \left(Q_{LCP_i}\right)_{min}\right] < \Delta Q_{Tol}$. Among them, h_i Q_{LCP_i}, $\left[\left(Q_{LCP_i}\right)_{max} - \left(Q_{LCP_i}\right)_{min}\right]$ are calculated by our model. Q_{iReq} and ΔQ_{Req} are the user defined parameters which should be given according various demands and circumstances.

To demonstrate the capability of LNDA in this study, we use the following battery working condition as the reference case. The heating power of the single battery is set to 700 W and the specific heat capacity of the working medium is 4.2 $kJ/(kg{\cdot}K)$. The comprehensive characteristics are detailed in S1.2. Consequently, the minimal flow rate Q_{iReq} is set to 7 L/min. To adhere to the temperature uniformity requirement of the entire system, another constraint demands that ΔQ_{Tol} should be $<$1.5 L/min [45]. The thermal distribution is obtained by COMSOL Multiphysics [46], with the details of simulation shown in S1.3. Notably, LNDA is designed to be a universal approach applicable to various types of BESSs. This includes different types of battery packs, varying structures of LCPs, and a range of operating conditions, such as temperature and humidity. To accommodate these diverse conditions, we adjust CONSTRAINT 2 accordingly.

2.2.3. Optimization goal

In the process of optimization, the Fitness function is designed to evaluate the economy of the liquid-cooling network [47]. Fitness function is a function related to (D, L, V, N, P), which consists of two parts [48] and can be expressed as follows

$$\mathrm{Fitness(D, L, V, N, P)} = \mathrm{C_1} + \mathrm{C_2} \tag{14}$$

where, C_1 is the total investment for the integrated energy storage liquid cold and heat management system, and C_2 is the system cost. The C_1 and C_2 are respectively calculated by the following formula

$$C_1 = \frac{r(1+r^t)}{(1+r)^t - 1}\sum_{i=1}^{n}\left[f(d_i)l_i + g(v_i)S_V\right] + \sum_{j=1}^{N_{pump}} W_i \tag{15}$$

$$C_2 = \sum_{j=1}^{N_{pump}} \frac{H_j \times Q_i}{\eta_{pi}} \cdot \tau \cdot c_e \times 10^{-7} + \alpha C_1 \tag{16}$$

where, r is the annual interest rate of the liquid-cooling network, t is the investment recovery time, d_i and l_i are the pipe diameter and flow. The pipe i cost can be calculated by the function $f(d_i)l_i$, which f can be expressed by $f(d_i) = c_a d_i + c_b$. $g(v_i)S_V$ is the total cost of valves, where $g(v_i)$ is the type of valve i and S_V is the price of the valve i. N_{pump} is the number of pumps, and W_i is the pump cost; H, Q, η_p are pump head, flow and efficiency, τ, c_e are annual working hours and electricity charges, and α is the depreciation rate of the network.

2.2.4. Optimization algorithm and designing process

To determine the optimization algorithm, the results of three different optimization algorithms are compared. The genetic algorithm (GA) is finally found as the best-suited algorithm [49], owing to its balance between efficiency and suitability. In GA, the maintenance of population diversity enables a systematic search for the global optimum. By evaluating and selecting adaptive function values, individuals displaying enhanced performance are prioritized and retained for the subsequent generation. The introduction of crossover and mutation operations facilitates the generation of novel gene combinations, thereby fostering population evolution and optimization. Through iterations, it progressively converges towards the identification of the chromosome parameter array that corresponds to the optimal fitness function value.

Based on the algorithm above, the process for LNDA is elucidated, and its flow chart is presented in Fig. 3c. The INPUTs of LNDA are the number of battery packs and their arrangement mode (written as an array). Initially, the graph of liquid-cooling network is formed according to the input. In the step of population initialization, each individual in the population is assigned an initial value in the form of $[D_1,\ldots,D_3,l_1,\ldots,l_n,V_1,\ldots,V_n,N_{pump},P_1,\ldots,P_N]$. In this notation, $D_1,\ldots,D_3$ denote the diameters of primary, secondary and tertiary pipes. $l_1,\ldots,l_n$ correspond to the lengths of each pipe, N_{pump} indicates the total number of booster pumps. $P_1,\ldots,P_N$ specify the positions of the pumps along the pipeline, identified by the serial number of the respective pipe. All these parameters are randomly generated within predefined constraints using a constrained random function, ensuring that each value adheres to the specified constraint ranges. Subsequently, the hydraulic performance, temperature uniformity and fitness function value are computed for each chromosome using the proposed hydraulic solution model. It is followed by CONSTRAINT 2. Then the chromosomes undergo selection, crossover, mutation, fitness recalculation, and cycle through this process [50]. During the crossover step, a crossover factor *mut* is introduced, and a random array is generated for the population. If a chromosome's responding value exceeds the crossover factor, it undergoes crossover with another randomly selected chromosome, starting at random nodes. During the mutation step, a mutation factor *acr* is introduced, with each chromosome node assigned a random value. If this value exceeds the mutation factor, the node is mutated by multiplying it by a random number. After a predefined number of iterations, the OUTPUTs of the chromosome parameter including the length and diameter of each pipeline, the opening of each valve, and the number and position of booster pumps corresponding to the optimal fitness function value is obtained.

2.3. Experimental method

A series of experiments are conducted to accomplish two primary objectives: (a). To validate the accuracy of our hydraulic model through experimental verification. (b). To assess and evaluate the efficiency and effectiveness of the LNDA. Based on the purposes above, two experimental rigs are established with specific functions. Rig 1 is dedicated to parameter measurement (Section 2.3.1), whereas Rig 2 is geared towards performance testing (Section 2.3.2). The experimental setups (Section 2.3.3) involve the utilization of both Rig 1 and Rig 2, which facilitate a comprehensive examination of objective 1 and 2.

2.3.1. Calculation parameter measurement

The experimental Rig 1 is designed and constructed to quantify the drag coefficients and characteristics of hydraulic components in the liquid-cooling network. It helps ensure the accuracy of parameters in the model. The measurement principle is depicted in Fig. 4a. It involves the measurement of the pressure difference in the fluid traversing the working element, monitored by a pilot gauge, followed by the assessment of flow rate using a flowmeter. The physical diagram of Rig 1 is illustrated in Fig. 4b. In the experiment, 20 °C water is selected as the working medium due to its common use and relevance. To ensure precision and reliability in the experimental measurements, a comprehensive dataset is collected. Following the experimental phase, resistance coefficients of the pipeline network elements are deduced through fitting procedures. These acquired coefficients are then utilized in the subsequent solution and optimization processes for the network.

2.3.2. Performance testing and evaluation

The experimental Rig 2 is designed and constructed to measure the hydraulic parameters and flow distribution in the operating system. It can be used to validate the model and evaluate the efficiency. The structure and components of the flow rate uniformity measurement rig are displayed in Fig. 4c-d, as the Fig. 4c shows the principle and layout of the rig: The working liquid, stored within the water tank, is propelled into the pipe network by the main pump. Consequently, the liquid is distributed to each LCP and subsequently passes through corresponding flowmeters before eventually returning to the tank, during which the flow rate within each LCP is assessed. The network is arranged with primary and secondary pipes. The primary pipeline is directly connected to the main pump, while the secondary pipes are connected to the LCPs. Valves are positioned at the center of the inlet secondary pipes, and flowmeters are placed at the center of the outlet secondary pipes. The sizes of the rig and LCPs are listed in Table 1. Fig. 4d shows the physical diagram of Rig 2, which consists of multiple layers of LCPs. Additionally, valves with adjustable opening and an S-shaped LCPs fabricated via CNC

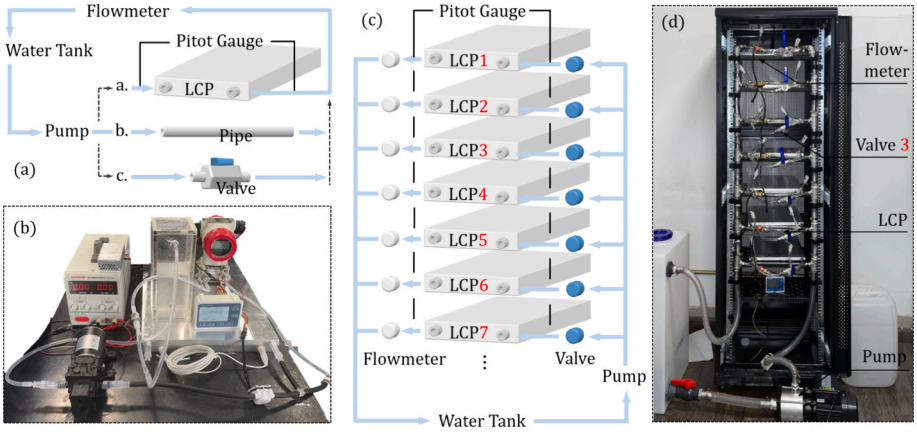

Fig. 4. (a) Schematic diagram of Rig 1 for measuring drag coefficient of pipeline network elements. (b) Physical diagram of the Rig 1. (c) Schematic diagram of Rig 2 for evaluating network performance. (d) Structure of Rig 2.

are used in the Rig 2. Through the experimental measurement, a comprehensive evaluation of the liquid cooling system's operational characteristics is conducted, which is further used to substantiate the accuracy of the model and efficacy of the LNDA.

2.3.3. Experimental setups: validation and evaluation

To verify the accuracy of the model, firstly, the drag coefficients of elements (valve, LCP, etc.) in the liquid-cooling network are measured by Rig 1. Subsequently, they are placed into our model code as inherent coefficients. A 7-step and an 8-step structure with all valves fully open are applied to the hydraulic solution model for calculation. Meanwhile, through the practical operation in Rig 2, the hydraulic performance of the 7-step and 8-step structure in the same operating conditions is experimentally measured. The experimental results are compared with the calculation results to validate the hydraulic solution model.

To evaluate the efficacy of the approach, LNDA is employed to optimize the flow distribution in the 7-step structure using Rig 2. In the optimization process, the openings of the 7 valves are chosen as the parameters to be optimized, and the objective function is defined as the difference between the maximum and minimum flow through different steps in the overall system. LNDA will output optimal valve opening values after optimization. Adjust the valves in Rig 2 according to these output values. Measure the flow distribution and compare them with the initial values to evaluate the accuracy of LNDA.

3. Results and discussion

3.1. Modeling validation

Following the setup in Section 2.3.3, model validation is conducted. Fig. 5(a-b) illustrates the drag coefficient and hydraulic performance across different elements. To accurately position the valve opening, ball valves with angular scale are adopted. By measuring the pressure drops at various flow rates, the hydraulic curve (Fig. 5a) can be precisely fitted using the form $\Delta P = C_v(i)Q^2$. $C_v(i)$ is the second term of Eq. (13) and represents the drag coefficient of the valve at the corresponding valve opening i (denoted as 1 minus the angular scale indicator divided by 90°). The hydraulic curves for various valve openings are first measured and fitted to obtain the C_v values at different valve openings i. Consequently, the curve of $C_v(i)$ versus i can be plotted and fitted, as shown in the upper left corner of Fig. 5a. As the valve opening i changes, the resistance coefficient of the valve adjusts according to the function $C_v(i)$, impacting the flow distribution across the entire cooling network. In the subsequent experiments, we optimized the valve openings as the key parameter to evaluate the performance of LNDA. The drag coefficient and hydraulic performance are also measured and fitted. Due to the low precision of CNC machining utilized here, the drag coefficients of the LCPs exhibit slight variations, despite having identical internal sizes and structures. These shortcomings are not expected to exist in industrial applications and industrialization. This is mainly because LCPs for industrial BESS are typically manufactured through stamping techniques, resulting in minimal differences among individuals. In the experiments, the 7-step structure contains LCP No. 1–7 from the highest layer to the lowest layer, and the 8-step structure contains LCP No. 1–8. The height difference between each layer is the same, which is 30 cm.

The parameters obtained by Rig 1 are input into the model, and the hydraulic performance of the 7-step and 8-step structure are solved and analyzed (Table 2). The solution process is displayed in Tables S2 and S3. Meanwhile, the hydraulic performances characterized by the flow rate of each LCP in two structures are measured. To avoid random results in the experiment, repeated measurements are performed by restarting the rig under the same conditions six times, and then the standard deviations of three measured values are calculated. Fig. 6 shows the hydraulic performances of 7-step and 8-step structures, respectively. The calculated values using our model show excellent agreement with the experiments. The computational results exhibit differences of 2.39 % and 3.23 % compared to the experimentally measured flow rates for 7-step and 8-step structures, respectively. The corresponding maximum errors across each step are 5.81 % and 5.83 %. Given the minute magnitude of errors, these results demonstrate excellent agreement with the present model. Moreover, the error analysis is also conducted to examine potential factors that could have contributed to the errors. These factors include ignoring pipe length cutting errors, slight bends in plastic pipes, drag coefficient measurement errors, and the inherent accuracy limitations of the instruments used. In practical applications, batch-cutting pipes, using metal pipes, and employing high-precision instruments can further improve the model accuracy.

3.2. Experimental evaluation of LNDA

The LNDA is then applied to the practical experimental system, and the approach is evaluated by following the setup in Section 3.3. In the untreated 7-step structure, hydraulic performance exhibits inhomogeneity, as illustrated by the varying flow rates across different steps (Fig. 6b). This disparity in flow rates can result in divergent thermal performances during practical applications. Here, the LNDA is applied to optimize the flow distribution in the 7-step structure.

Fig. 6c provides a comprehensive overview of the entire optimization

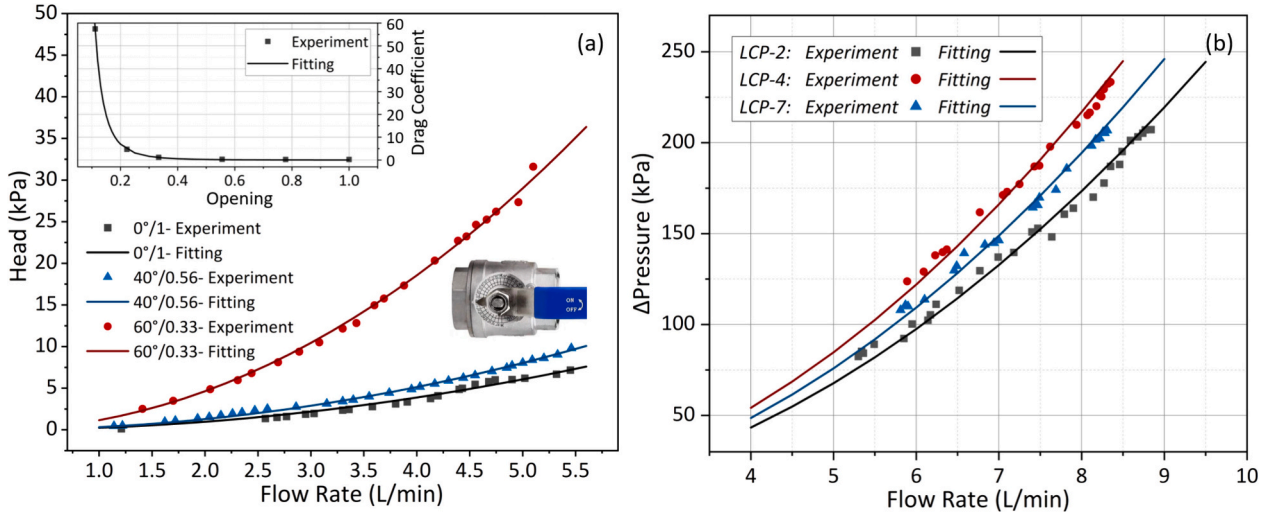

Fig. 5. (a) The hydraulic curve and drag coefficient of the valve at various opening positions (b) the hydraulic performance of different LCP (selected).

Table 2
Drag coefficients of LCPs and various valve openings.

LCP number	1	2	3	4	5	6	7	8
Drag coeff.	3.117	2.709	2.085	3.389	3.327	2.97	3.037	6.65
Valve degree	0°/1	20°/0.78	40°/0.56		50°/0.44	60°/0.33	70°/0.22	80°/0.11
Drag coeff.	0.243	0.249	0.321		0.406	1.160	4.701	57.46

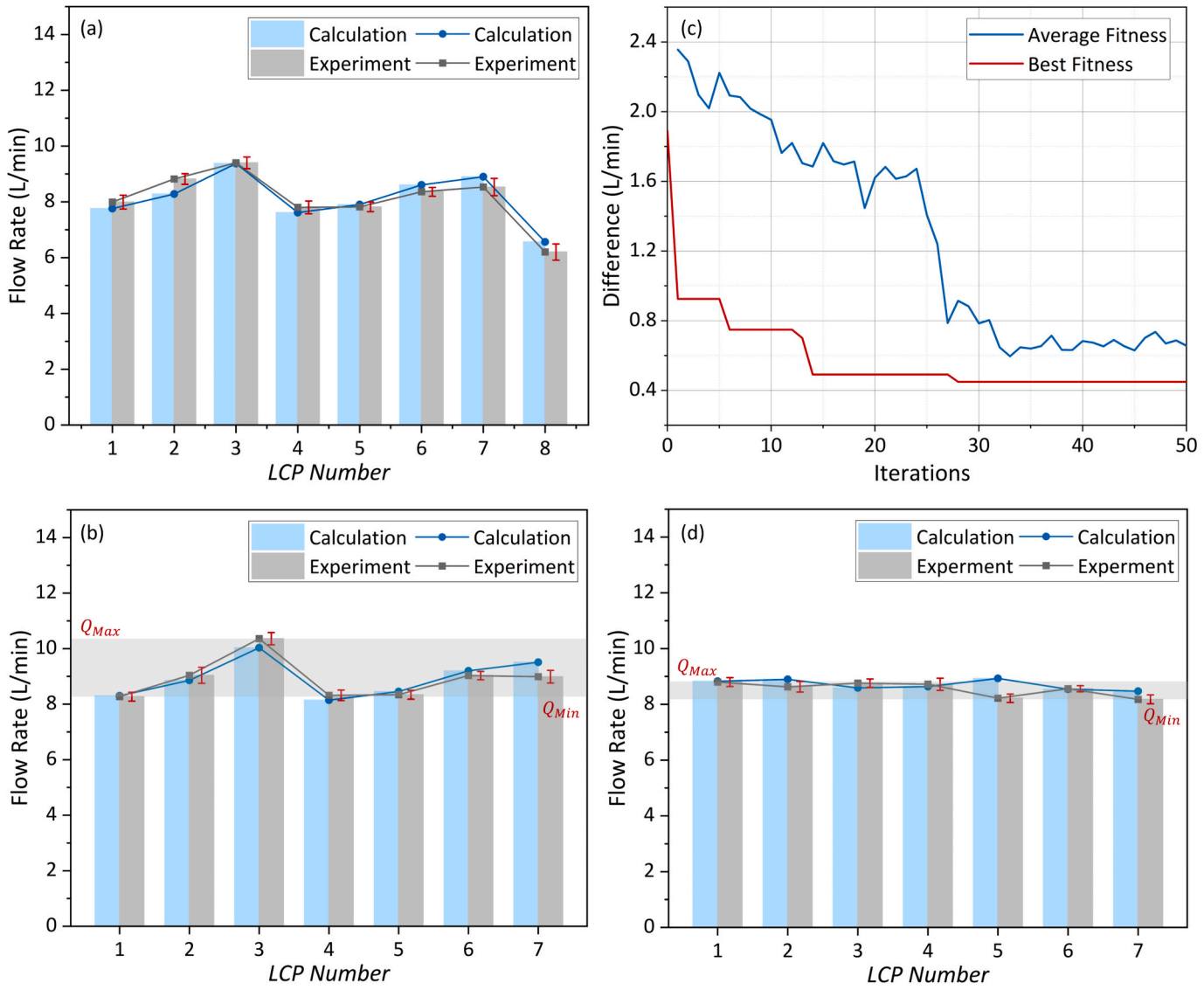

Fig. 6. The comparation of flow rate between the experiments and calculations in (a) 8-step structure (b) 7-step structure to validate the model To evaluate the efficiency of LNDA, the (c) optimizing process of 7-step structure and (d) flow distribution after optimization.

process, which necessitates only 34.6 s for the completion of 50 iterations with the population of 50 and the attainment of the desired system consistency. Throughout this process, the average value of the objective function for the population (Average Fitness) demonstrates a converging trend. Significantly, the optimal value for the objective function (Best Fitness) reveals a discernible decreasing trend with each iteration, diminishing from 1.89 to 0.45, a decrease of 76.2 %. The optimization procedure ultimately culminates in the identification of the optimal chromosome, characterized by the valve degrees [60° 45° 55° 0° 35° 55° 55°]. Smaller valve degrees correspond to greater flow rates, with 0° indicating a fully open valve.

The non-optimized flow distribution within the 7-step structure is illustrated in Fig. 6b, where the abscissa represents the number of LCPs in the structure and the ordinate depicts the corresponding flow rates. Prior to optimization, all valve degrees are set to 0° (fully open). The initial computational results (depicted in blue) reveal that the maximum and minimum flow rates are 10.03 *L/min* and 8.14 *L/min*. The experimental data (depicted in grey) indicate maximum and minimum flow rates of 10.36 *L/min* and 8.27 *L/min* before the optimization, with a deviation of 2.09 *L/min*.

After the optimization, the optimized valve degrees above are implemented in the experimental rig to measure the flow distribution and assess the efficacy of the optimization. The post-optimized flow distribution is presented in Fig. 6d, where the calculation results indicate that the maximum and minimum flows are 8.93 *L/min* and 8.47 *L/min*. Similarly, experimental data show that the maximum and minimum

flow are respectively 8.80 *L/min* and 8.18 *L/min*, with a deviation of 0.62 *L/min*. The upper boundary of the shallow-grey region signifies the maximum flow measured through the LCP in the experiment, while the lower boundary indicates the minimum value. Notably, a distinct consistency becomes apparent upon examining the shallow grey areas in Fig. 6b and c. The optimization process results in a 70.3 % reduction in the practical flow heterogeneity, and all values exceed the ideal flow rate for uniform heat in a single battery pack.

3.3. Application for large-scale energy storage station

In the preceding Section 3.2, we explore the application of the LNDA in a miniaturized BESS structure (capable of accommodating single-digit battery packs), complemented by experimental results. However, larger energy storage stations with the capacity for dozens/hundreds of battery packs exist in practical scenarios, prompting us to employ this approach for the design and optimization of such configurations. Moreover, when investigating systems with an equivalent quantity of battery packs, our inquiry encompasses the exploration of diverse pack arrangements. The significance of studying diverse battery pack configurations lies not only in determining the spatial arrangement of pipes but also in influencing the total number of pipes and other pertinent parameters within the system.

3.3.1. Effect of the quantity of battery packs

The LNDA is conducted with a variable number of battery packs, denoted as $N = 24$, 30, 36 and 42. As the quantity of battery packs increases, it is notable that they are not uniformly arranged in a single row but rather dispersed across multiple rows. Additionally, the pipelines are categorized into primary (main pipeline, connected to the main pump), secondary, and tertiary pipelines (linked with the LCP). Consequently, the battery arrangement modes are selected as A_N = [6 6 6 6], [6 6 6 6 6], [6 6 6 6 6 6] and [6 6 6 6 6 6 6] respectively. Fig. 7g-h shows the structural sketch of the liquid-cooling network for the case of $N = 30$, 36, with the arrangement mode remaining analogous under varying conditions. For different quantities and arrangements of battery packs, the network will vary. Assuming there are N battery packs divided into m rows, with an arrangement described by $A = [n_1, n_2, \ldots, n_m]$, where $n_1 + n_2 + \ldots + n_m = N$. The total number of nodes and pipelines can be calculated as $2\,m + 2\,N$ and $2\,m\text{-}1 + 3\,N$, respectively. In the supporting information Section S1.1, we outline how to mathematically describe different pipe network structures in the code and perform subsequent calculations in detail.

In the optimization process, the size of the population is 50 and the iteration step is 60. The optimization curve is shown in Fig. 7a. In these processes, the optimal fitness value demonstrates an increase with the increase of *N*, albeit not in a linear fashion. Observations reveal that the greater the value of N, the slower the rate of increase in fitness. However, the efficiency of LNDA is enhanced within this range, as the ratios of initial fitness value to the optimal ones are 42.6 %, 21.8 %, 24.2 % and 20.8 % at $N = 42$, 36, 30, and 24 [51]. The total pump power of the system is reduced through optimization. Before optimization, the pump power requirements for $N = 24$, 30, 36, 42 are 3.96 *kW*, 6.23 *kW*, 7.99 *kW*, and 13.52 *kW*, respectively. After optimization, these values are reduced to 3.68 *kW*, 5.06 *kW*, 7.35 *kW*, and 9.17 *kW*, respectively. Fig. 7b shows the valve opening values before and after the LNDA. Meanwhile, we examined the optimized flow distribution (Fig. 7c-f), discovering minimal variation in flow among LCPs, which is within 1.5 *L/min*. Consequently, this results in a uniform temperature distribution. We also demonstrate the temperature uniformity in case N = 24 by simulation results, with the details discussed in Supporting information S2. After optimization, the temperature uniformity has been improved, which helps to avoid the capacity loss in the operation. This adherence to design and application specifications attests to the effectiveness of the optimization process.

3.3.2. Effect of the distribution of battery packs

Our investigation also extends to exploring the influence of various arrangement modes on the liquid-cooling network. In this analysis, we specifically choose $N = 30$ and categorize the battery packs into three types of distribution modes: decreased arrangement (A_1 = [8 7 6 5 4]), sub-uniform arrangement (A_2 = [8 8 8 6], A_3 = [6 4 6 4 6 4]), and uniform arrangement (A_4 = [6 6 6 6 6], A_5 = [5 5 5 5 5 5]). The basic graph is displayed in Fig. 8b-f. These distinct arrangement modes

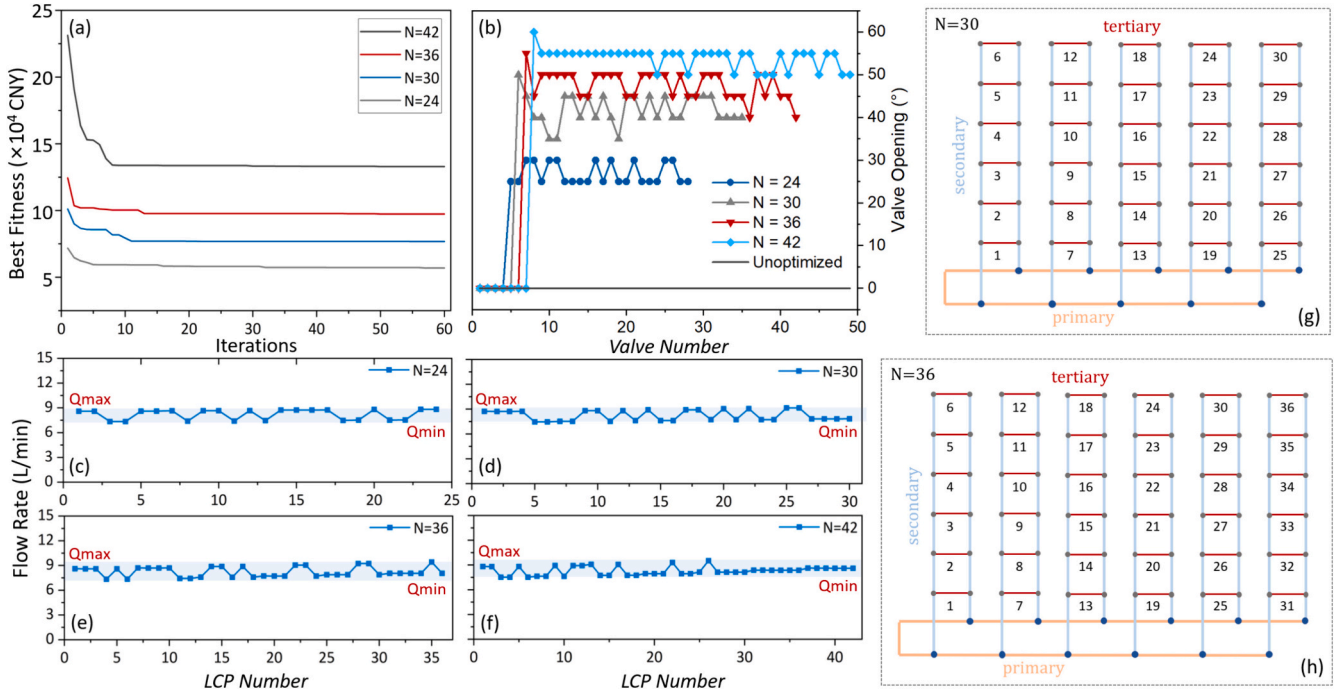

Fig. 7. (a) Optimizing process of different battery packs number $N = 24$, 30, 36, 42. (b) Valve opening value before and after the LNDA. (c-f) Flow distribution through LCPs of different battery packs number. (g-h) Structural sketch of Liquid-cooling network at $N = 30$, 36.

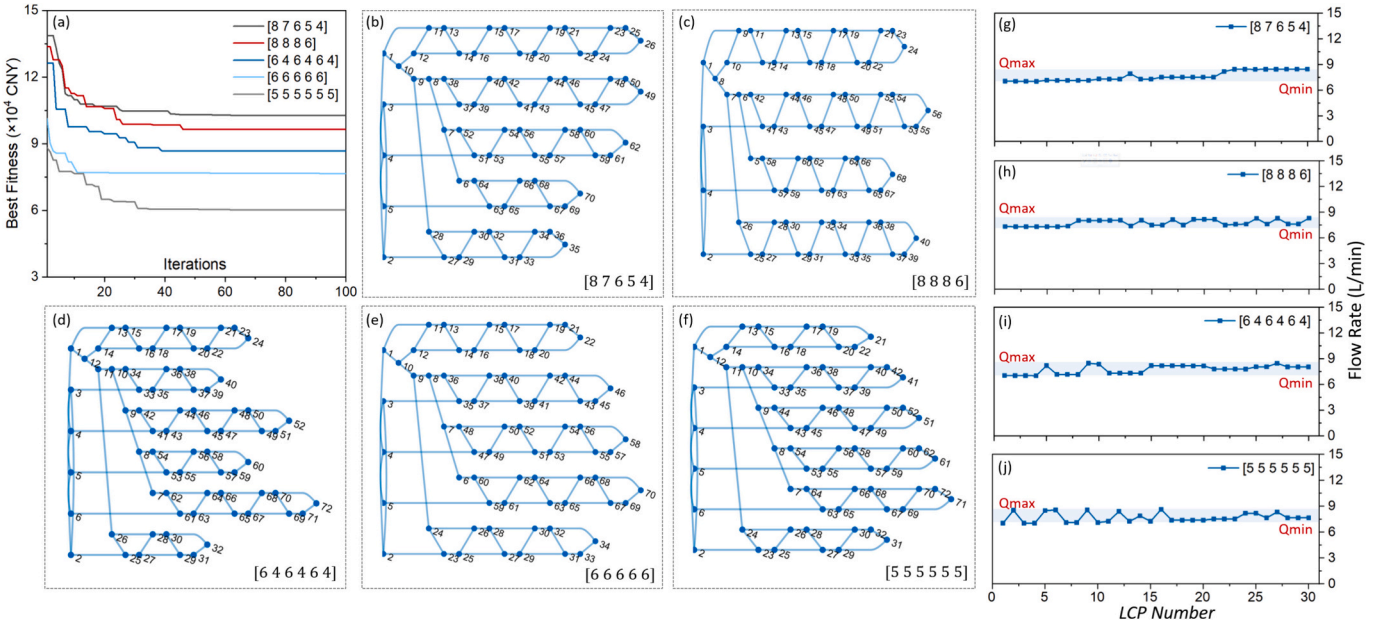

Fig. 8. (a) Optimizing process of different battery pack arrangement modes. (b-f) Basic graphs of different battery pack arrangement modes. (g-j) Flow distribution through LCPs of different battery pack arrangement modes.

undergo thorough comparative analysis to elucidate their respective impacts on the overall system.

In the optimization process, the size of the population is 50 and the iteration step is 100. The optimization curve is shown in Fig. 8a. Meanwhile, the flow distribution (Fig. 8g-j) is examined, discovering minimal variation in flow among LCPs, which is within 1.5 *L/min*. While the total flow rates of the system vary slightly in different arrangement modes (233.15, 232.56, 228.92, 241.91, 231.36 *L/min* from A_1 - A_5), the economic cost of the liquid cooling network differs considerably among different arrangement modes. From Fig. 8a, it becomes evident that the optimal economic performance of the system is achieved when the battery packs are evenly distributed. The economic optimization of LNDA shows high efficiency, with values of 26.0 %, 27.9 %, 31.3 %, 24.2 %, and 31.7 % from A_1 to A_5. Additionally, in the case of even distribution, the arrangement of [5 5 5 5 5 5] is more economical than [6 6 6 6 6], which can be attributed to the fact that there is smaller pressure loss caused by fewer battery packs arranged in each row.

4. Conclusion

This investigation presents an efficient liquid-cooling network design approach (LNDA) for thermal management in battery energy storage stations (BESSs). LNDA can output the full range of optimal parameters for the liquid-cooling network only with the inputs of the number and arrangement of battery packs. The designed network can ensure an ideal, uniform flow distribution and the lowest system cost in BESSs, thereby enhancing their benefits as well as ensuring their safety and efficient operation.

LNDA is constructed on our developed graph-based hydraulic solution model of liquid-cooling network combined with genetic algorithm optimization. The graph-based hydraulic model has high accuracy, in agreement of >96 % with experimental results. LNDA shows notable effectiveness and efficiency, taking only 34.6 *s* to improve the flow uniformity of the practical system by 70.3 %. LNDA also demonstrates wide applicability in large-scale BESS with varying numbers of battery packs, where the economic efficiency can be improved by 20–40 % and the high uniformity of the system can be ensured.

The impact of varying battery pack arrangements on the economic viability and thermal uniformity of BESSs is also analyzed using LNDA. Results reveal that the uniform arrangement outperforms non-uniform arrangements in both economic efficiency and thermal uniformity. Within a uniform arrangement, a configuration with fewer battery packs in each row proves to be more advantageous for system operation. The proposed approach and findings offer valuable insights that can contribute to the advancement of energy storage systems and related technologies.

For the current LNDA, there is still room for improvement in allowing optimization based on the number of battery packs, rather than requiring a predefined arrangement mode to design and optimize the liquid cooling network. Moreover, LNDA's versatility makes it a promising candidate for application in liquid-cooling thermal management systems across various fields, such as data centers. LNDA has also demonstrated the potential for temperature control in BESSs. The direction of our future work focuses on leveraging LNDA's rapid optimization capabilities to swiftly respond to temperature fluctuations within the BESSs, thereby achieving effective system temperature control.

CRediT authorship contribution statement

Huaiyu Zuo: Writing – original draft, Validation, Project administration, Methodology, Investigation, Formal analysis, Data curation, Conceptualization. **Jiacheng Han:** Writing – review & editing, Validation, Data curation. **Song Xue:** Investigation, Data curation. **Zhaochen Wang:** Writing – review & editing, Methodology. **Zeyu Wang:** Writing – review & editing. **Run Hu:** Writing – review & editing, Funding acquisition. **Jinlong Ma:** Writing – review & editing, Supervision. **Xiaobing Luo:** Writing – review & editing, Supervision, Funding acquisition, Conceptualization.

Declaration of competing interest

The authors declare that they have no known competing financial interests or personal relationships that could have appeared to influence the work reported in this paper.

Data availability

Data will be made available on request.

Acknowledgements

The authors would like to acknowledge the financial support by National Key R & D Project from Ministry of Science and Technology of China (Grant No. 2022YFA1203100).

Appendix A. Supplementary data

Supplementary data to this article can be found online at https://doi.org/10.1016/j.est.2024.113866.

References

[1] J. Hjalmarsson, K. Thomas, C. Boström, Service stacking using energy storage systems for grid applications – a review, J. Energy Storage 60 (2023) 106639.
[2] X.J. Han, T.M. Ji, Z.K. Zhao, H. Zhang, Economic evaluation of batteries planning in energy storage power stations for load shifting, Renew. Energy 75 (2015) 643–647.
[3] S.A. Khan, S. Ahmad, K.T. Lau, K. Dong, S. He, H. Liu, J. Zhao, A novel strategy of thermal management system for battery energy storage system based on supercritical CO2, Energy Convers. Manag. 277 (2023) 116676.
[4] T. Weitzel, M. Schneider, C.H. Glock, F. Löber, S. Rinderknecht, Operating a storage-augmented hybrid microgrid considering battery aging costs, J. Clean. Prod. 188 (2018) 638–654.
[5] Y.Q. Chen, Y.Q. Kang, Y. Zhao, L. Wang, J.L. Liu, Y.X. Li, Z. Liang, X.M. He, X. Li, N. Tavajohi, B.H. Li, A review of lithium-ion battery safety concerns: the issues, strategies, and testing standards, J. Energy Chem. 59 (2021) 83–99.
[6] S. Ma, M.D. Jiang, P. Tao, C.Y. Song, J.B. Wu, J. Wang, T. Deng, W. Shang, Temperature effect and thermal impact in lithium-ion batteries: a review, Prog. Nat. Sci-Mater. Int. 28 (6) (2018) 653–666.
[7] S. Nyamathulla, C. Dhanamjayulu, A review of battery energy storage systems and advanced battery management system for different applications: challenges and recommendations, J. Energy Storage, 86(A):111179.
[8] Y. Ma, Y.Q. Liu, H. Ding, X.H. Yu, Hierarchical optimal intelligent battery thermal management strategy for an electric vehicle based on ant colony sliding mode control, ISA T. 143 (2023) 477–491.
[9] C.X. Wu, Y.L. Sun, H. Tang, S.W. Zhang, W. Yuan, L.K. Zhu, Y. Tang, A review on the liquid cooling thermal management system of lithium-ion batteries, Appl. Energy 375 (2024) 124173.
[10] Y. Zhang, L. Song, J. Tian, W. Mei, L. Jiang, J. Sun, Q. Wang, Modeling the propagation of internal thermal runaway in lithium-ion battery, Appl. Energy 362 (2024) 123004.
[11] Y. Jin, Z.X. Zhao, S. Miao, Q.S. Wang, L. Sun, H.F. Lu, Explosion hazards study of grid-scale lithium-ion battery energy storage station, J. Energy Storage 42 (2021) 102987.
[12] X.N. Feng, C.S. Xu, X.M. He, L. Wang, G. Zhang, M.G. Ouyang, Mechanisms for the evolution of cell variations within a LiNixCoyMnzO2/graphite lithium-ion battery pack caused by temperature non-uniformity, J. Clean. Prod. 205 (2018) 447–462.
[13] A. Greco, X. Jiang, D. Cao, An investigation of lithium-ion battery thermal management using paraffin/porous-graphite-matrix composite, J. Power Sources 278 (2015) 50–68.
[14] Y.F. Lv, X.W. Geng, W.M. Luo, T.Y. Chu, H.N. Li, D.F. Liu, H. Cheng, J. Chen, X. He, C.C. Li, Review on influence factors and prevention control technologies of lithium-ion battery energy storage safety, J. Energy Storage 72 (B) (2023) 108389.
[15] R. Zhao, S. Zhang, J. Liu, J. Gu, A review of thermal performance improving methods of lithium ion battery: electrode modification and thermal management system, J. Power Sources 299 (2015) 557–577.
[16] D. Chen, J. Jiang, G. Kim, C. Yang, A. Pesaran, Comparison of different cooling methods for lithium ion battery cells, Appl. Therm. Eng. 94 (2016) 846–854.
[17] N.A. Pambudi, A. Sarifudin, R.A. Firdaus, D.K. Ulfa, I.M. Gandidi, R. Romadhon, The immersion cooling technology: current and future development in energy saving, Alex. Eng. J. 61 (12) (2022) 9509–9527.
[18] L.F. Cabeza, A. Frazzica, M. Chàfer, D. Vérez, V. Palomba, Research trends and perspectives of thermal management of electric batteries: bibliometric analysis, J. Energy Storage 32 (2020) 101976.
[19] T. Deng, G. Zhang, Y. Ran, Study on thermal management of rectangular Li-ion battery with serpentine-channel cold plate, Int. J. Heat Mass Transf. 125 (2018) 143–152.
[20] F.R. Zhang, Z.K. Huang, Sh.Y. Li, S.Z. Sun, H.B. Zhao, Design and thermal performance analysis of a new micro-fin liquid cooling plate based on liquid cooling channel finning and bionic limulus-like fins, Appl. Therm. Eng. 237 (2024) 121597.
[21] A.H. Mohammed, R. Esmaeeli, H. Aliniagerdroudbari, M. Alhadri, S.R. Hashemi, G. Nadkarni, S. Farhad, Dual-purpose cooling plate for thermal management of prismatic lithium-ion batteries during normal operation and thermal runaway, Appl. Therm. Eng. 160 (2019) 114106.
[22] L.W. Jin, P.S. Lee, X.X. Kong, Y. Fan, S.K. Chou, Ultra-thin minichannel LCP for EV battery thermal management, Appl. Energy 113 (2014) 1786–1794.
[23] Y.C. Wang, X.B. Xu, Z.W. Liu, J.Z. Kong, Q.W. Zhai, H. Zakaria, Q.Z. Wang, F. Zhou, H.Y. Wei, Optimization of liquid cooling for prismatic battery with novel cold plate based on butterfly-shaped channel, J. Energy Storage 73 (D) (2023) 109161.
[24] J.K. Xie, Y.J. Luo, G.Q. Zhang, C.M. Mo, X.Q. Yang, Compact design of integrated battery thermal management systems enabled by bi-functional heating-cooling plates and temperature-equalizing strategy, Renew. Energy 222 (2024) 119909.
[25] F.R. Zhang, X.L. Lu, L. Zhang, K. Xiao, F. Lu, Y.X. He, Y.L. Zhu, H. Gou, Bionic liquid cooling plate thermal management system based on flow resistance-thermal resistance model, Int. J. Therm. Sci. 190 (2023) 108336.
[26] H. Chen, D. Li, Current status and challenges for liquid-cooled data centers, Front. Energy Res. 10 (2022) 952680.
[27] P. Shahi, A.P. Deshmukh, H.Y. Hurnekar, S. Saini, P. Bansode, R. Kasukurthy, D. Agonafer, Design, development, and characterization of a flow control device for dynamic cooling of liquid-cooled servers, ASME. J. Electron. Packag. 144 (4) (2021) 041008.
[28] N.K. Mdachi, C. Choong-koo, Comparative review of thermal management systems for BESS, Batteries 10 (7) (2024) 224.
[29] T. Waldmann, M. Wilka, M. Kasper, M. Fleischhammer, M. Wohlfahrt-Mehrens, Temperature dependent ageing mechanisms in lithium-ion batteries - a post-mortem study, J. Power Sources 262 (2014) 129–135.
[30] A. Almoli, A. Thompson, N. Kapur, J. Summers, H. Thompson, G. Hannah, Computational fluid dynamic investigation of liquid rack cooling in data centres, Appl. Energy 89 (1) (2012) 150–155.
[31] H. Kwon, J. Cho, S.C. Sung, H.M. Kim, S.K. Lee, H. Park, Conceptual thermal design for 40 ft container type 3.8 MW energy storage system by using computational simulation, Sustain Energy Technol Assess 56 (2023) 103075.
[32] M. Li, S. Ma, H. Jin, R. Wang, Y. Jiang, Performance analysis of liquid cooling battery thermal management system in different cooling cases, J. Energy Storage 72 (2023) 108651.
[33] J. Yu, Q. Liu, A. Zhao, S. Chen, Z. Gao, F. Wang, R. Zhang, A distributed optimization algorithm for the dynamic hydraulic balance of chilled water pipe network in air-conditioning system, Energy 223 (2021) 120059.
[34] W. Zhang, X. Chen, J. Liu, W. Yu, Pipeline design and simulation analysis of power battery liquid cooling system, Chinese Battery Industry 26 (1) (2022) 1–5.
[35] C. Pistoresi, Y.L. Fan, L.G. Luo, Numerical study on the improvement of flow distribution uniformity among parallel mini-channels, Chem. Eng. Process. Process Intensif. 95 (2015) 63–71.
[36] F. Chen, Y. Liu, Z. Cui, W. Shao, An optimization method for uniform flow distribution in the manifold of server cabinet, Energy Sci. Eng. 9 (2021) 390–401.
[37] R. Raoni, A.R. Secchi, E.C. Biscaia, Novel method for looped pipeline network resolution, Comput. Chem. Eng. 96 (2017) 169–182.
[38] D. Brki'c, Iterative methods for looped network pipeline calculation, Water Resour. Manag. 25 (2011) 2951–2987.
[39] P. Amal, K. Ajish, An algorithm for kth minimum spanning tree, Electron Notes Discrete Math. 53 (2016) 343–354.
[40] A. Kathapurkar, R. Montgomery, Spanning trees in dense directed graphs, J. Comb. Theory. Ser. B 156 (2022) 223–249.
[41] K. Takata, Space-optimal, backtracking algorithms to list the minimal vertex separators of a graph, Discret. Appl. Math. 158 (2010) 1660–1667.
[42] P.F. Boulos, D.J. Wood, Explicit calculation of pipe-network parameters, J. Hydraul. Eng. 116 (1990) 1329–1344.
[43] R.Z. Zhang, M.Y. Lu, W.W. Yang, L.X. Liang, Q. Xu, Validation of 3D multi-physics equivalent resistance network model with flow field for VRFB stack and battery scale-up analysis, J. Energy Storage 90 (2024) 111768.
[44] K. Haghighi, R. Mohtar, V.F. Bralts, L.J. Segerlind, A linear formulation model for pipe network components, Comput. Electron. Agric. 7 (4) (1992) 301–321.
[45] K. Yang, Y. Li, J. Yuan, M. Cheng, M. Liu, C. Kang, H. Shi, Y. Jiang, A thermal management system for an energy storage battery container based on cold air directional regulation, J. Energy Storage 61 (2023) 106679.
[46] M. Li, S.M. Ma, H. Jin, R.J. Wang, Y. Jiang, Performance analysis of liquid cooling battery thermal management system in different cooling cases, J. Energy Storage 72 (D) (2023) 108651.
[47] W. He, S. Ding, J. Zhang, C. Pei, Z. Zhang, Y. Wang, H. Li, Performance optimization of server water cooling system based on minimum energy consumption analysis, Appl. Energy 303 (2021) 117620.
[48] J. Zeng, J. Han, G. Zhang, Diameter optimization of district heating and cooling piping network based on hourly load, Appl. Therm. Eng. 107 (2016) 750–757.
[49] L. Su, T. Nie, C.O. Ho, Z. Yang, P. Calvez, R.K. Jain, B. Schwegler, Optimizing pipe network design and central plant positioning of district heating and cooling system: a graph-based multi-objective genetic algorithm approach, Appl. Energy 325 (2022) 119844.
[50] Y. Wang, J. Wang, M. Gao, D. Zhang, Y. Liu, Z. Tan, J. Zhu, Cost-based siting and sizing of energy stations and pipeline networks in integrated energy system, Energy Convers. Manag. 235 (2021) 113958.
[51] C. Pan, Z. Jia, J. Wang, L. Wang, J. Wu, Optimization of liquid cooling heat dissipation control strategy for electric vehicle power batteries based on linear time-varying model predictive control, Energy 283 (2023) 129099.